Article

Electrokinetic Nanorod Translocation through a Dual-Nanopipette

Xiaoling Zhang, Yaqi Bai, Shiping Liu, Jun Yang, and Ning Hu*

Read Online

ACCESS | Metrics & More | Article Recommendations | SI Supporting Information

ABSTRACT: Glass nanopipettes, as important sensing tools, have attracted great interest due to their wide range of applications in detecting single molecules, nanoparticles, and cells. In this study, we investigated the translocation behavior of nanorod particles through dual-nanopipettes using a transient continuum-based model based on an arbitrary Lagrangian−Eulerian approach. Our findings indicate that the translocation of nanorods is slowed down in the dual-nanopipette system, especially in the dual-nanopipette system with a nanobridge. These results are in qualitative agreement with previous experimental findings reported in the literature. Additionally, the translocation of nanorods is influenced by factors such as bulk concentration, initial location of the nanorod, and surface charge of the nanopipette. Notably, when the surface charge density of the nanopipette is relatively high and the initial location of the nanorod is in the reservoir, the nanorod can hardly enter the nanopipette, resulting in a relatively low translocation efficiency. However, the translocation efficiency can be improved by initially positioning the nanorod in one of the barrels. The resulting dual-blockade current signal can be used to correlate the characteristics of the nanorod.
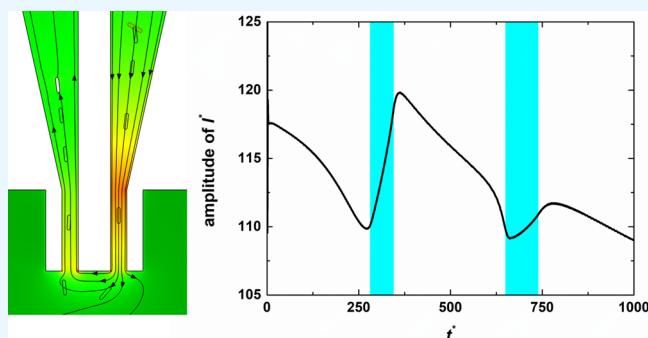
INTRODUCTION

Inspired by the ion channels on biomembranes, nanodevices such as nanopores, nanochannels, and nanopipettes have drawn much interest over the past few decades.[1−7] These nanodevices have the potential to create innovative molecular delivery systems and chemical/biosensors by imitating biological ion channels.[8] As a simple and powerful sensing technique, glass nanopipettes can detect specific nanoparticles by measuring changes in the ionic current passing through them. This includes DNA/RNA molecules,[9,10] proteins,[11−13] and organic polymers. The conical shape and narrow tip of the nanopipette create a confined region, which enhances the electrochemical field within the pipet. This improved electrochemical confinement effect enables the monitoring of analyte properties in the form of ion signals.[14] Nanopipettes are also widely used as probes for scanning electrochemical microscopy and scanning ion conductance microscopy.[15−17] In addition to single nanopipettes, dual and multichannel nanopipettes have also been employed as new tools in several fields.[18−24] Recently, Cadinu et al.[25] proposed dual nanopores (also known as double-barrel nanopores or theta-pipettes) separated by constructing zeptoliter nanobridges to trap and detect single molecules, resulting in a three-order of magnitude decrease in molecular velocity compared to traditional nanopores. Furthermore, they reported a new strategy for manipulating single molecules in double-barrel nanopores that enabled novel modes of molecular transport control, demonstrating the platform's ability to effectively bridge molecules between two nanopores and actively control DNA transport.[26] By employ-ing four-channel nanopipettes, they created a programmable multinanopore structure with four neighboring, individually configurable nanochannels to control the dynamics of DNA.[23] These new approaches have significantly broadened the application of nanopipettes. For example, dual-nanopipettes have found utility in electrochemical single-cell protein therapeutics and other applications.[27] By using a θ-nano-pipette, Zhang et al.[28] established a single-cell resistive-pulse sensing method for an important DNA repair protein, along with evaluating related drugs.

In addition to the growing number of applications for nanopipettes, the fundamental understanding of nanopipettes is also constantly being achieved. The structure of nanopipettes is more complicated compared to ordinary cylindrical nanopores, resulting in more intricate ion transport and particle translocation behavior. Recently, McPherson et al.[29] discovered the occurrence of a second kind of electroosmosis in nanopipettes. At high surface charge densities and large applied potentials, this kind of EOF prevents dye entry from the bath into the nanopipette, regardless of the potential polarity.[29] In addition, Yu and co-workers[30] explored the particle transport behavior at the nanopipette orifice by

combining the results of experiments with those from finite element modeling. They developed a principle of access resistance for single-particle analysis at the opening of a nanopipette.[31,32] Additionally, they observed a strong correlation between the particle's surface charge and the angle θ, which is associated with the asymmetry of the current spike.[33] We studied the ion transport characteristics of double-barrel nanopores and identified the presence of two ion-enriched zones and two ion-depleted zones within them.[34]

To effectively utilize nanodevices, it is crucial to have modeling and simulations that provide clear insights into the electrokinetic translocation of nanoparticles through these devices. Inadequate knowledge of dynamic particle motions leads to ineffective particle manipulation in addition to placing restrictions on the amount and quality of information that may be gathered.[35] However, current studies have primarily focused on particle translocation through nanochannels or nanopores.[36−39] The dynamic analysis of nanoparticles or DNA molecules passing through dual-nanopipettes has not been performed through numerical simulation. Therefore, this study aims to systematically investigate the dynamic transport behaviors of nanorod particles through dual-nanopipettes using a transient continuum-based model. This model is defined within an arbitrary Lagrangian−Eulerian (ALE) framework and includes the Nernst−Planck equations, the Poisson equation, and the Navier−Stokes equations. Some translocation phenomena of nanorods in nanopipettes, which are different from those in ordinary cylindrical nanopores, have been found.

MATHEMATICAL MODEL

To reduce computing effort, we model the nanopipette system as a two-dimensional geometry. The system consists of a dual-nanopipette immersed in a large reservoir with a width of $2 \times W$ and a height of H, as shown in Figure 1. Figure 1
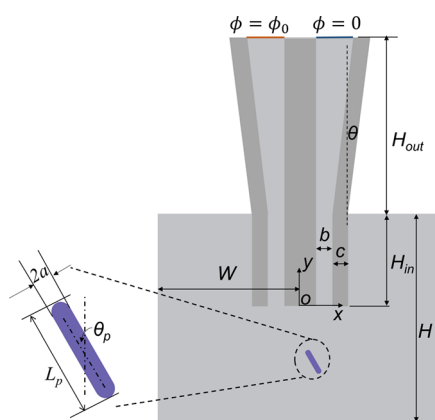

Figure 1. Illustrations of the nanorod translocation through the dual-nanopipette. The dark gray parts represent the walls of the dual-nanopipette, and the light gray part represents the simulation domain. The purple one is the nanorod.

schematically depicts a dual-nanopipette, where the tip contains two nanochannels with a width of b, a wall thickness of c, and a gap of $2 \times c$ between the two barrels. The insertion part of the nanopipette, which does not change in size, has a length of H_{in}, representing the narrow section of the nanopipette. The outer part of the nanopipette, with a cone angle of θ, has a length of H_{out}. A binary KCl aqueous solution,

with the properties of permittivity ε_f, dynamic viscosity μ, and density ρ, is present throughout the entire system. The origin of the Cartesian coordinate system (x, y) used for describing all the variables in the current investigation is set at the midpoint of the nanopipette tip. We construct a negatively charged nanorod particle composed of a rectangle and two semicircles with a radius of a. The nanorod has a length of L_p and an angle of θ_{p0} with regard to the y-axis at its initial location of (x_{p0}, y_{p0}). We define $\theta_{p0} > 0$ in the case of a clockwise angle relative to the y-axis and *vice versa*. The two barrels of the dual-nanopipette are subject to an applied potential difference ϕ_0. Thus, an electric field is generated across the dual-nanopipette, which leads to the translocation of the negatively charged nanorods. Simultaneously, an ionic current flows from the anode barrel to the cathode barrel through the dual-nanopipette.

In the electrolyte solution, the electrostatics are regulated by the Poisson equation, and the ionic mass transport is regulated by the Nernst−Planck equations:

$$-\varepsilon_0 \varepsilon_f \nabla^2 \phi = \rho_e = F \sum_{i=1}^{2} c_i z_i \tag{1}$$

$$\frac{\partial c_i}{\partial t} + \nabla \cdot \mathbf{N}_i = 0 \tag{2}$$

$$\mathbf{N}_i = \mathbf{u}c_i - D_i \nabla c_i - z_i \frac{D_i}{RT} F c_i \nabla \phi \ (i = 1 \text{ and } 2) \tag{3}$$

where c_i, z_i, $\mathbf{N}_i$, and D_i are the molar concentration, the valence, the ionic flux density, and the diffusivity of the ith ion, respectively (i.e., cation K$^+$ for $i = 1$ and anion Cl$^-$ for $i = 2$), in the electrolyte solution. ρ_e is the space charge density of mobile ions; ε_0 and ε_f represent the absolute permittivity of the vacuum and the relative permittivity of the electrolyte, respectively; ϕ represents the electric potential within the fluid; $\mathbf{u}$ represents the fluid velocity; F represents the Faraday constant; R represents the universal gas constant; and T represents the absolute temperature of the electrolyte solution. In the dual-nanopipette system, the potential difference between the two barrels is $\phi = 0$ on the blue line and $\phi = \phi_0$ on the orange line, as shown in Figure 1. The wall of the nanopipette and the surface of the nanorod carry the specified charge densities σ_w (i.e., $-\mathbf{n} \cdot \nabla \phi = \sigma_w/(\varepsilon_0 \varepsilon_f)$) and σ_p (i.e., $-\mathbf{n} \cdot \nabla \phi = \sigma_p/(\varepsilon_0 \varepsilon_f)$). Here, the unit normal vector $\mathbf{n}$ points toward the fluid from the respective boundary. The rest of the boundaries are considered to be uncharged. The ionic concentrations at the openings of the reservoir and the openings of the nanopipettes have the boundary conditions $c_i = C_0$ ($i = 1$ and 2), respectively, with the assumption that the top opening(s) of the nanopipettes is relatively larger than that of the tip. On each of the other boundaries, the normal ionic fluxes are set to zero.

Moreover, fluid motion is regulated by the Navier−Stokes equations, and the inertia of these equations is ignored because the electrokinetic flow in nanofluidics has a quite low Reynolds number, given as

$$\rho \frac{\partial \mathbf{u}}{\partial t} = -\nabla p + \mu \nabla^2 \mathbf{u} + \mathbf{F}, \text{ in } \Omega_f \tag{4}$$

$$\nabla \cdot \mathbf{u} = 0, \text{ in } \Omega_f \tag{5}$$

$$\mathbf{F} = -\rho_e \nabla\phi = -\left(F\sum_{i=1}^{N} c_i z_i\right)\nabla\phi \tag{6}$$

where p is the pressure. At the openings of the reservoir and the openings of the nanopipettes, normal flows with $p = 0$ are imposed. The surfaces of the nanopipette are subject to a nonslip boundary condition. The other boundaries of the reservoir are subject to slip boundary conditions. The movement of the nanorods can be divided into translation and rotation; hence, the following is the flow boundary condition for the nanorod surface:

$$\mathbf{u} = \mathbf{U}_p + \boldsymbol{\omega}_p \times (\mathbf{x}_s - \mathbf{x}_p) \tag{7}$$

where $\mathbf{U}_p$ denotes the translational velocity and $\boldsymbol{\omega}_p$ denotes the rotational velocity; the location vectors $\mathbf{x}_s$ and $\mathbf{x}_p$ correspond to the nanorod surface and center, respectively.

According to Newton's second law, $\mathbf{U}_p$ can be determined by

$$m_p \frac{d\mathbf{U}_p}{dt} = \mathbf{F}_{total} \tag{8}$$

$\mathbf{F}_{total}$ is the total force exerted on the nanorod, which is composed of the hydrodynamic force $\mathbf{F}_H$ and the electrical force $\mathbf{F}_E$, that is

$$\mathbf{F}_{total} = \mathbf{F}_H + \mathbf{F}_E \tag{9}$$

$$\mathbf{F}_H = \int \mathbf{T}^H \cdot \mathbf{n} d\Gamma = \int [-p\mathbf{I} + \mu(\nabla\mathbf{u} + \nabla\mathbf{u}^T)] \cdot \mathbf{n} d\Gamma \tag{10}$$

$$\mathbf{F}_E = \int \mathbf{T}^E \cdot \mathbf{n} d\Gamma = \int \varepsilon_0\varepsilon_f\left[\mathbf{E}\mathbf{E} - \frac{1}{2}(\mathbf{E}\cdot\mathbf{E})\mathbf{I}\right]\cdot\mathbf{n} d\Gamma \tag{11}$$

The hydrodynamic and Maxwell stress tensors are represented in these equations by $\mathbf{T}^H$ and $\mathbf{T}^E$, respectively. $\mathbf{E}$ denotes the electric field and can be calculated by $\mathbf{E} = -\nabla\phi$.

The nanorod's rotational velocity, $\boldsymbol{\omega}_p$, can be determined by

$$I_p \frac{d\omega_p}{dt} = \int (\mathbf{x}_s - \mathbf{x}_p) \times (\mathbf{T}^H \cdot \mathbf{n} + \mathbf{T}^E \cdot \mathbf{n}) d\Gamma \tag{12}$$

where I_p is the moment of inertia of the nanorod.

The nanorod's center of mass $\mathbf{x}_p$ and orientation $\boldsymbol{\theta}_p$ can be determined by

$$\mathbf{x}_p = \mathbf{x}_{p0} + \int_0^t \mathbf{U}_p dt \tag{13}$$

$$\theta_p = \theta_{p0} + \int_0^t \omega_p dt \tag{14}$$

where $\mathbf{x}_{p0}$ and $\boldsymbol{\theta}_{p0}$ are the initial location and orientation of the nanorod, respectively.

When the nanorod passes through the dual-nanopipette, the ionic current induced through the nanopipette is

$$I = \int F\left(\sum_{i=1}^{2} z_i \mathbf{N}_i\right)\cdot\mathbf{n} dS \tag{15}$$

where S denotes either the surface of the anode or cathode due to current conservation ($\frac{\partial \rho_e}{\partial t} + \nabla\cdot\mathbf{J} = 0$, $\mathbf{J}$ is the current density). In this study, we can obtain a reduced current due to the 2-D geometry. During the computation, to normalize all the governing equations listed above, the particle radius a is

selected as the length scale, RT/F as the potential scale, the bulk concentration C_0 as the ionic concentration scale, $U_0 = \varepsilon_0\varepsilon_f R^2 T^2/(\mu a F^2)$ as the velocity scale, and $\mu U_0/a$ as the pressure scale. Thus, the above governing equations have been normalized as

$$-\nabla^{*2}\phi^* = \frac{(\kappa a)^2}{2}\sum_{i=1}^{2} c_i^* z_i \tag{16}$$

$$\frac{\partial c_i^*}{\partial t^*} + \nabla^*\cdot(\mathbf{u}^* c_i^* - D_i^*\nabla^* c_i^* - z_i D_i^* c_i^* \nabla^*\phi^*) = 0 \tag{17}$$

$$Re\frac{\partial\mathbf{u}^*}{\partial t^*} + \nabla^* p^* - \nabla^{*2}\mathbf{u}^* = -\frac{(\kappa a)^2}{2}\sum_{i=1}^{2} c_i^* z_i \nabla^*\phi^* \tag{18}$$

$$\nabla^*\cdot\mathbf{u}^* = 0 \tag{19}$$

where $\kappa^{-1} = \lambda_D = \sqrt{\varepsilon_0\varepsilon_f RT/(2F^2 C_0)}$ is the Debye length and $Re = \rho U_0 a/\mu$ is the Reynolds number.

The following dimensionless boundary conditions are applied:

$$\phi^* = \phi_0^* \text{ (orange lines) or 0 (blue lines)} \tag{20}$$

$$-\mathbf{n}\cdot\nabla^*\phi^* = \sigma_p^* \text{ on the nanorod surface} \tag{21}$$

$$-\mathbf{n}\cdot\nabla^*\phi^* = \sigma_w^* \text{ on the nanopipette wall} \tag{22}$$

$$c_i^* = 1 \text{ at the reservoir and nanopipette openings} \tag{23}$$

$$\mathbf{u}^* = \mathbf{U}_p^* + \omega_p^* \times (\mathbf{x}_s^* - \mathbf{x}_p^*) \text{ on the nanorod surface} \tag{24}$$

The dimensionless equations for nanorod motion are

$$m_p^*\frac{d\mathbf{U}_p^*}{dt} = \int (\mathbf{T}^{H*}\cdot\mathbf{n} + \mathbf{T}^{E*}\cdot\mathbf{n}) d\Gamma^* \tag{25}$$

$$I_p^*\frac{d\omega_p^*}{dt} = \int (\mathbf{x}_s^* - \mathbf{x}_p^*) \times (\mathbf{T}^{H*}\cdot\mathbf{n} + \mathbf{T}^{E*}\cdot\mathbf{n}) d\Gamma^* \tag{26}$$

$$\mathbf{T}^{H*} = -p^*\mathbf{I} + (\nabla^*\mathbf{u}^* + \nabla^*\mathbf{u}^{*T}) \tag{27}$$

$$\mathbf{T}^{E*} = \mathbf{E}^*\mathbf{E}^* - \frac{\mathbf{E}^*\cdot\mathbf{E}^*}{2}\mathbf{I} \tag{28}$$

The dimensionless ionic current flowing through the nanopipette normalized by $FU_0 C_0 a^2$ is

$$I^* = \int\left(\sum_{i=1}^{2} z_i \mathbf{N}_i^*\right)\cdot\mathbf{n} dS^* \tag{29}$$

NUMERICAL IMPLEMENTATION AND CODE VALIDATION

COMSOL Multiphysics (www.comsol.com) was used to solve this strongly coupled model. The coupled PNP and NS equations have been previously demonstrated to exhibit satisfactory sensitivity in studying particle translocation through a nanopore.[40] Our model is based on the ALE approach, which can effectively capture the translocation behaviors of particles in the computational domain and has been employed by other researchers with consistent findings.[41−44] In our model, the electric potential and concen-

tration were discretized using quadratic elements, while the fluid behavior was discretized using P2+P1 elements. To ensure accurate results, an extremely fine mesh was applied to the nanorod surface and nanopipette wall. A mesh range of 10,000 to 45,000 elements was utilized to guarantee full convergence and mesh independence (Figure S1). Figure S1 demonstrates the convergence of corresponding values and satisfactory result stability, with differences within 5% as the total number of meshes increases. To further confirm the validity of the developed model, we investigated the y-component velocity of nanorods through dual-nanopipettes. There are three configurations using a dual-nanopipette: (i) a conventional single nanopipette configuration, (ii) a dual-nanopipette configuration without a nanobridge (in the reservoir), and (iii) a nanobridge configuration.[25] The simulation domains can be found in Figures 1 and S2. It is assumed that the wall of the nanopipette is uncharged ($\sigma_w^* = 0$) to eliminate the influence of surface charge density on the wall of the nanopipette and focus solely on the influence of the configuration. The initial location of the nanorod in the conventional single nanopipette configuration and dual-nano-pipette configuration without a nanobridge is in the large reservoir, and that in the dual-nanopipette configuration with a nanobridge is in the cathode barrel. Figure 2 shows the
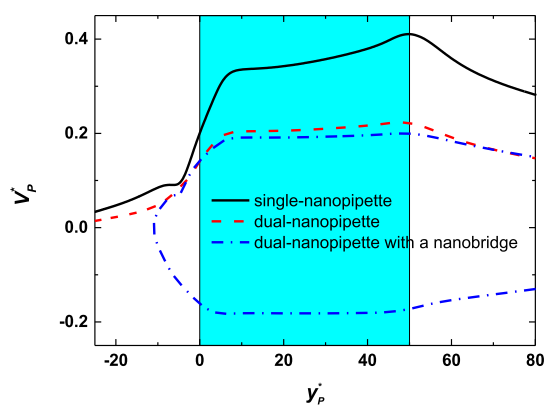

Figure 2. Nanorod's y-component translational velocity, V_P^*, vs its location, y_P^*, in the single-nanopipette (solid line in black), dual-nanopipette (dashed line in red), and dual-nanopipette with a nanobridge (dash-dotted line in blue). $C_0 = 100$ mM ($\kappa a = 1.0265$), $\phi_0 = 5$ V ($\phi_0^* = 193.41$). The blue part is the narrow section of the nanopipette (y^* is between 0 and 50).

relationship between the nanorod's location y_P^* and its y-component translational velocity V_P^* in the three configurations. To facilitate a straightforward comparison, Figure 2 shows that at the midpoint of the nanopipette insertion ($y_P^* = 25$), the y-component translational velocity of the nanorods in the conventional single-nanopipette configuration is approximately 0.35, that in the dual-nanopipette configuration is 0.21, and that in the dual-nanopipette configuration with a nanobridge is 0.19. Notably, in the dual-nanopipette with a nanobridge configuration, the y-component translational velocity of the nanorods is the lowest. This implies that in the dual-nanopipette with a nanobridge, the velocity of nanorods passing through it is reduced, which is qualitatively consistent with experimental results.[25] The reason that the nanorod is slowed down in the dual-nanopipette is that the electric field is nearly half that of a single nanopipette (Figure S3). On the other hand, in the case of dual-nanopipettes with

nanobridges, the nanorods, being similar in size to both the nanopipette tip and the nanobridge, experience a current blockade in both the barrels and the nanobridge (Figure S4). This leads to a longer dwell distance and increased detection time. However, this velocity has not been reduced to 3 orders of magnitude as mentioned in the literature,[25] as we only considered the simplest case at this stage, ignoring factors such as the surface charge density of the nanopipette and the crowding and tangling of molecules in the actual experiments.

■ RESULTS AND DISCUSSION

In the present study, we investigate the second configuration as this configuration is more commonly used for dual-nano-pipettes. As shown in Figure 1, the whole domain, including the reservoir and the dual-nanopipette, is filled with KCl electrolyte solution. The width of the reservoir is $2 \times W = 300$ nm, and the height is $H = 200$ nm. The width and wall thickness of the nanochannels on the nanopipette tip are $b = 10$ and $c = 10$ nm, respectively. The heights of the insertion part and the outer part of the nanopipette are $H_{in} = 50$ nm and $H_{out} = 200$ nm. The outer part of the nanopipette features a cone angle of θ ($\sim 12.4°$). The nanorod has a length of $L_p = 10$ nm, and the semicircles have a radius of $a = 1$ nm. The surface of the nanorod has a constant charge density of $\sigma_p = -0.01$ C/m^2. The values of several physical parameters are as follows: $\rho = 1 \times 10^3$ kg/m^3, $\varepsilon_f = 80$, $\varepsilon_0 = 8.854 \times 10^{-12}$ F/m, $\mu = 1 \times 10^{-3}$ Pa·s, $D_1(K^+) = 1.95 \times 10^{-9}$ m^2/s, $D_2(Cl^-) = 2.03 \times 10^{-9}$ m^2/s, $T = 300$ K, $F = 96485.3415$. The translocation behaviors of a nanorod through dual-nanopipettes are studied as a function of these parameters: the bulk concentration C_0, the applied electric field, the surface charge density of the dual-nanopipette σ_w, and the initial location of the nanorod (x_{p0}^*, y_{p0}^*).

Effect of the Bulk Concentration, C_0. We first investigate how the bulk concentration affects the nanorod's y-component velocity when applying two distinct electric fields, $\phi_0 = 0.1$ V ($\phi_0^* = 3.8682$) (Figure 3A) and $\phi_0 = 10$ V ($\phi_0^* = 386.82$) (Figure 3B) through dual-nanopipettes in a large reservoir. In this section, it is assumed that the wall of the nanopipette is uncharged ($\sigma_w^* = 0$). The nanorod's initial location is (x_{p0}^*, y_{p0}^*) = (0, −30); that is, the nanorod is in the large reservoir. The concentration influences the thickness of the electric double layer (EDL). When the EDLs of the particle and nanopore overlap, it leads to significant electrostatic interactions that affect the translocation process. For bulk concentrations of C_0 = 100 mM, 10 mM, and 1 mM, the ratios of the nanorod radius to the Debye length, κa, are 1.0265, 0.32, and 0.10265, respectively. When the applied electric field is relatively low ($\phi_0 = 0.1$ V in Figure 3A) and the bulk concentration is relatively high (dashed line: $C_0 = 10$ mM and dash-dotted line: $C_0 = 100$ mM), the nanorod successfully passes through the nanopipette. However, when the concentration is relatively low (solid line: $C_0 = 1$ mM), the nanorod stops at the nanopipette orifice (see Supporting Material Movie 1), which is similar to the observation that nanorods cannot pass through ordinary cylindrical nanopores under low bulk concentration and applied electric field conditions.[44] When the applied voltage increases 100 times to $\phi_0 = 10$ V, the velocity of the nanorods increases approximately 100 times. At $C_0 = 1$ mM, the nanorods are not trapped and can enter the nanopipettes at a high velocity. That is, under the condition of a large voltage, the larger the concentration, the slower the translational velocity. This phenomenon is also consistent with that of
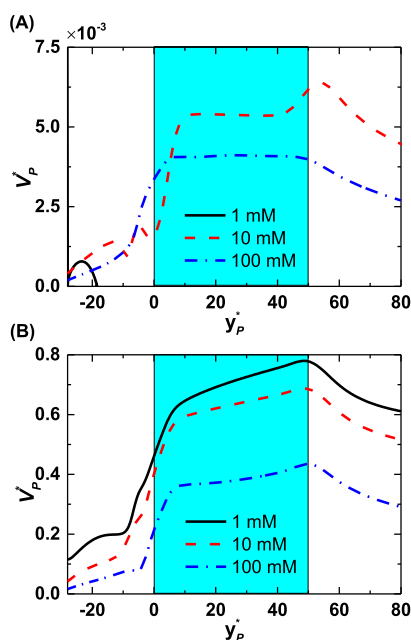
Figure 3. Nanorod's y-component translational velocity, V_P^*, vs its location, y_P^*, when $\phi_0 = 0.1$ V ($\phi_0^* = 3.8682$) (A) and $\phi_0 = 10$ V ($\phi_0^* = 386.82$) (B). Solid lines in black, dashed lines in red, and dash-dotted lines in blue represent, respectively, $C_0 = 1$ mM, 10 mM, and 100 mM ($\kappa a = 0.10265$, 0.32, and 1.0265). The blue part is the narrow section of the nanopipette (y^* is between 0 and 50).

Figure 4. Nanorod's y-component translational velocity, V_P^*, vs its location, y_P^*, in the dual-nanopipette under $\phi_0 = 10$ V when $C_0 = 10$ mM (A) and $C_0 = 100$ mM (B). Solid lines in black, dashed lines in red, and dash-dotted lines in blue represent, respectively, $\sigma_w = 0$, -0.002 C/m^2 and 0.002 C/m^2. The blue part is in the narrow section of the nanopipette (y^* is between 0 and 50).

ordinary cylindrical nanopores and has been explained in previous studies because particles with a fixed surface charge density have an increased zeta potential as κa decreases.[44] Consequently, the velocity of the nanorod increases with decreasing bulk concentration. However, it is worth noting that the particles could be trapped at the nanopipette orifice when the concentration is relatively high ($C_0 = 100$ mM) if a larger voltage, such as 20 V, is applied (see Supporting Material Movie 2). Additionally, in the conventional single nanopipette configuration, the nanorod cannot enter the nanopipette when $C_0 = 100$ mM and ϕ_0 exceeds a critical value (see Supporting Material Movie 3). This finding deviates from our general understanding that a stronger electric field facilitates easier entry into the nanopore. This is because, except for electroosmotic flow, which is always the opposite of electrophoresis for balancing the force acting on the nanorod when the nanopipette is uncharged (Figure S5), nanorods also experience negative dielectrophoresis, pushing the nanorod away from the tip of the nanopipette.

Effect of the Surface Charge Density of the Nanopipette, σ_w. In nanopore/nanopipette sensing, the surface charge density on the walls of the nanopore/nanopipette may strongly affect the translocation of particles due to the generation of an EOF, especially when the electric double layers of the nanorod and the nanopore/nanopipette overlap and under a relatively low electric field.[44] Thus, we investigate the effect of the surface charge density. Through a series of simulation studies, the influence of the surface charge density can be divided into two cases.

When the surface charge density of the nanopipette is relatively low (± 0.002 C/m^2), the surface charge can promote (0.002 C/m^2) or hinder (-0.002 C/m^2) the translocation of particles. Figure 4 shows the relationship between the y-component translational velocity V_P^* and the nanorod location
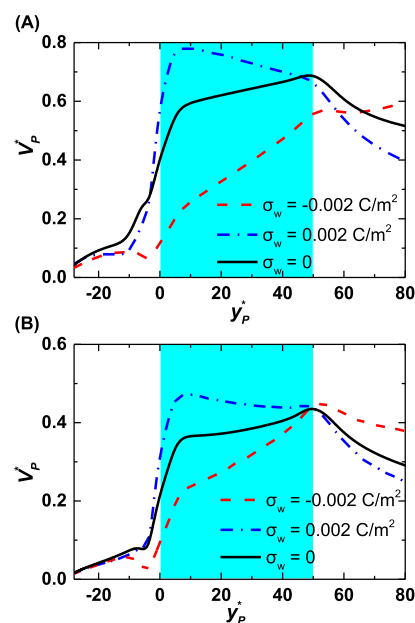
y_P^* under $\phi_0 = 10$ V when $C_0 = 10$ mM (Figure 4A) and $C_0 = 100$ mM (Figure 4B). When the surface of the nanopipette is negatively (positively) charged, the direction of EOF is in opposition to (consistent with) that of electrophoresis. Therefore, V_P^* is less (greater) than when the surface of the nanopipette is uncharged. This is also consistent with the phenomenon of ordinary nanopores. However, this trend changes in the opposite direction after passing through the narrow section (i.e., when $y^* > 50$). When the surface of the nanopipette is negatively charged (-0.002 C/m^2), V_P^* increases when they enter the narrow section but decreases after passing through the narrow section. When the nanopipette surface is negatively charged (-0.002 C/m^2), V_P^* becomes the largest. To further understand these behaviors, the flow fields around the particles are shown in Figure 5. The direction of the flow field changes due to the interaction between the nanopipette and the negatively charged nanorod after the nanorod enters the nanopipette, so V_P^* increases.

Additionally, we investigate the situation in which $\phi_0 = 0.1$ V, $C_0 = 10$ mM and 100 mM. The electric field and flow field in the nanopipette are significantly influenced by the surface charge density of the nanopipette, making it a challenge for particles to enter the nanopipette, except for when $C_0 = 100$ mM and $\sigma_w = -0.002$ C/m^2. Because the applied voltage is low, the flow plays a major role in driving the particles to move in the streamline direction. However, in these cases, the applied electric field can be appropriately increased to increase the probability of particles entering the nanopipette.

When we continue to increase the surface charge density, such as to ± 0.005 C/m^2, it becomes difficult for the nanorods to enter the nanopipette (Figure S6A,B), and the nanorods move away from the tip of the nanopipette under the action of fluid, which leads to a low capture efficiency of the nanopipette. This is different from that of ordinary cylindrical nanopores. In a single cylindrical nanopore, when the
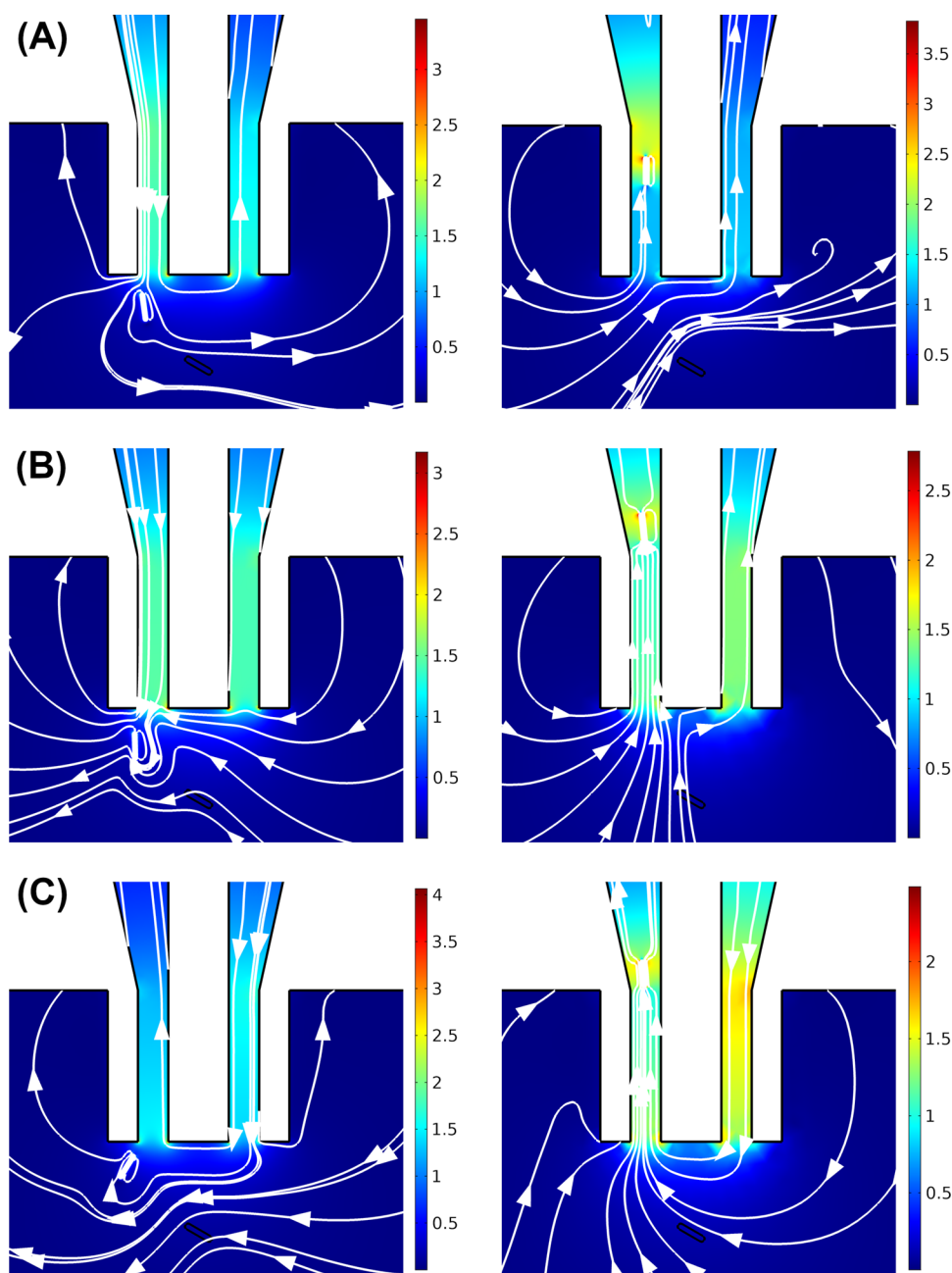
Figure 5. Spatial distributions of the intensity of the electric field $|E^*|$ and flow field around the particle under $\phi_0 = 10$ V and $C_0 = 100$ mM. (A) $\sigma_w = -0.002$ C/m^2, (B) $\sigma_w = 0$, (C) $\sigma_w = 0.002$ C/m^2. The color bars represent $|E^*|$, and the arrowed lines represent the streamlines of the flow field.

nanopore surface charge density is positive, the direction of EOF is consistent with the direction of electrophoresis, and the capture efficiency is usually improved. To further understand these behaviors, the flow field around the particle is shown in Figure S6C,D. Figure S6C,D shows that although the direction of EOF in the nanopipette is the same as that of electrophoresis (0.005 C/m^2) or the opposite (-0.005 C/m^2), most streamlines do not enter the nanopipette. Moreover, the greater the surface charge density of the nanopipette, the greater the effect of EOF, resulting in the particle not entering the nanopipette. The same phenomenon also occurs when a single nanopipette is used and when $C_0 = 100$ mM.

It can be noticed that although the translational velocity of nanorods can be reduced in dual-nanopipettes, when we study the influence of surface charge on particle translocation, we

also find that the translocation efficiency is not high when using a single-nanopipette or dual-nanopipette, especially when the surface charge density is relatively high. We can consider changing the surface charge by chemical modification to minimize the surface charge density before the experiments. For dual-nanopipettes, in addition to chemical modification methods, we propose a new method to improve the translocation efficiency, which is discussed in the next subsection.

Effect of the Initial Location of the Nanorod, (x_{p0}^*, y_{p0}^*). The initial location of the nanorods also affects their translocation.[44] In the dual-nanopipettes, the particles could be in the reservoir or in the barrels. Figures S7 and S8 show the results for the initial location of the nanorod in the cathode barrel, that is, $(x_{p0}^*, y_{p0}^*) = (25, 150)$, when the nanopipette is
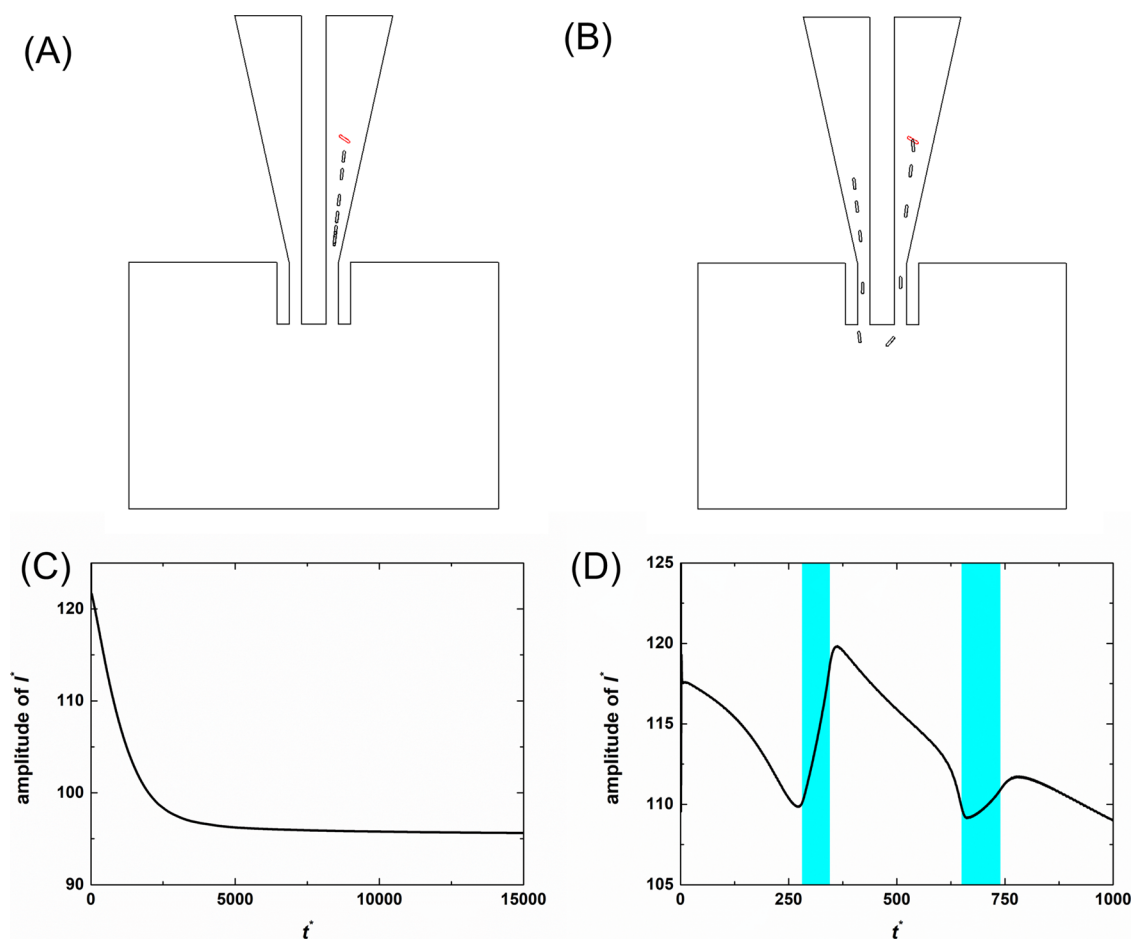
Figure 6. Trajectories of the nanorod and the reduced current through the nanopipette bearing a relatively large surface charge density under $\phi_0 =$ 10 V, $C_0 = 100$ mM at $(x_{p0}^*, y_{p0}^*) = (25, 150)$. (A) Trajectories of the nanorod when $\sigma_w = -0.005$ C/m^2, (B) trajectories of the nanorod when $\sigma_w =$ 0.005 C/m^2, (C) the reduced current when $\sigma_w = -0.005$ C/m^2, and (D) the reduced current when $\sigma_w = 0.005$ C/m^2. The red one is at the initial location. The blue part is in the narrow section of the nanopipette (y^* is between 0 and 50).

uncharged or bears a relatively small charge density (± 0.002 C/m^2), respectively. In most cases, the nanorods translocate from the cathode barrel to the anode barrel, except for when $\sigma_w = 0$, $\phi_0 = 0.1$ V, and $C_0 = 1$ mM. We compare the flow fields between $C_0 = 1$ mM and 10 mM (Figure S6). When $C_0 = 1$ mM, the EOF in the cathode barrel is in opposition to the direction of nanorod motion; when $C_0 = 10$ mM, the EOF is the same as the direction of nanorod motion. Thus, the nanorods could be trapped in the barrel when $C_0 = 1$ mM. Compared with the results when σ_w is 0 and ± 0.002 C/m^2, when $\sigma_w = 0$, the concentration is lower and the velocity is faster in both barrels. However, when the surface charge is not equal to 0, the opposite trend occurs in the anode barrel after the nanorods pass through the narrow section (Figure S9). The reason has been discussed in the previous subsection (Figure 5). Meanwhile, when the aperture of the nanopipette is relatively small, the nanorod is difficult to enter the nanopipette when the initial location of the nanorod is in the reservoir $(x_{p0}^*, y_{p0}^*) = (0, -30)$. However, when the initial location of the nanorod is in the barrel $(x_{p0}^*, y_{p0}^*) = (25, 150)$, the nanorod can pass through the two barrels when $\sigma_w = 0.002$ C/m^2, while the nanorod can only pass through one barrel and stop at the orifice of the nanopipette when $\sigma_w = -0.002$ C/m^2 (Table S1).

The translocation of nanorods differs when a nanopipette has a relatively large surface charge density. Figure 6 shows the

trajectories of the nanorods and the reduced current through the dual-nanopipette with a relatively large surface charge density. When σ_w is negative and relatively large ($\sigma_w = -0.005$ C/m^2), the EOF's direction differs from that of the electrophoresis, and the EOF force defeats the electrical driving force; then, the nanorod may become stuck in the cathode barrel; that is, the nanorod cannot translocate to the other barrel (Figure 6A). Thus, when $\sigma_w = -0.005$ C/m^2, a long-term ionic current blockade occurs (Figure 6C). When σ_w is positive, due to the EOF occurring in the same direction as the electrophoresis, the nanorods can be completely transported from the cathode barrel to the anode barrel (Figure 6B). When $\sigma_w = 0.005$ C/m^2, the translational velocity of the nanorod is greater than that when $\sigma_w = 0.002$ C/m^2 because the effect of EOF increases with increasing surface charge density. Comparing Figures 6 to S6, it can be found that the initial location of the nanorod could also affect the translocation behavior of the nanorod. Thus, to improve the potential low translocation efficiency of the nanopipettes mentioned earlier, the nanorods can be put in one of the barrels at the beginning.

Figure 6D shows the amplitude of the ionic current when the nanorod is translocated through the dual-nanopipette with $\sigma_w = 0.005$ C/m^2. Two ionic current blockades are formed during the process of nanorod transport from the cathode barrel to the anode barrel. This is because the size of nanorods

is equivalent to that of nanopipette tips. When the nanorod is in the nanopipette, an ionic current blockade will be formed. When the particle is in the reservoir, because the nanorod is too small relative to the reservoir, an ionic current blockade cannot be formed. Thus, two blockades will be formed during the whole translocation process. This phenomenon was not observed in previous experiments because long DNA was usually used to conduct experiments with dual-nanopipettes, and the DNA did not leave the nanopipette completely; thus, a current similar to that of a single nanopipette or dual-nanopipette with a nanobridge would form. However, this resulting dual-blockade current signal can potentially be used to analyze the characteristics of nanorods twice, and the correlation of them, potentially increasing the accuracy of the analysis. On the other hand, the second blockade is smaller than the first blockade, which is different from when the surface charge density is relatively small (Figure S10). Additionally, after the nanorod passes through the narrow section, the current tends to continue to decrease because of the increased cross-sectional area. These changes in ion current can be explained by ion transmission. Figure S11 shows the distribution of the dimensional concentration of K^+ (Figure S11A) and Cl^- (Figure S11B) when the nanorod passes through the nanopipette. Taking K^+ ions as an example, we analyze ion transport in dual-nanopipettes. Because the nanorod is negatively charged, it is surrounded by many positive ions, that is, K^+ ions, so that when the nanorod enters the anode barrel, the nanorod tends to bring K^+ ions into the anode barrel. Since the nanopipette is positively charged, the basic direction of electroosmotic flow is from the cathode to the anode (Figure 5C), which also transports K^+ ions into the anode barrel, and the larger the surface charge density is, the more severe this effect will be. Both effects are opposite to the ionic current's overall flow direction, so the current will be reduced.

CONCLUSIONS

In this study, we developed a transient continuum-based model to investigate the translocation behaviors of nanorods through dual-nanopipettes. The model comprises the Nernst–Planck equations, the Poisson equation, and the Navier–Stokes equations, and the ALE method was used to solve it. Although our model is simplified to a two-dimensional representation, it allows us to qualitatively analyze the translocation of nanorods within the nanopipette and draw the following conclusions:

1. Compared to that of a single nanopipette, under the same conditions, the translocation of nanorods could be slowed down in the dual-nanopipettes, especially in cases where nanobridges are present, which qualitatively agrees with the experimental observations.

2. In a dual-nanopipette without a nanobridge, when the nanorod is initially placed in the reservoir connecting the dual-nanopipette, the translocation efficiency is adversely reduced, especially if the surface of the nanopipette has a relatively high charge density.

3. The translocation efficiency can be improved by positioning the particle initially in one of the barrels, during which the nanorod is successfully transported from one barrel through the reservoir and enters the other barrel, even when the charge density on the nanopipette surface is relatively high. During this translocation process, the resulting ionic current history

exhibits two blockades, corresponding to the nanorod exiting one barrel to the reservoir and entering the other barrel from the reservoir. The resulting dual-blockade current signal may be used to correlate the characteristics of the nanorod.

ASSOCIATED CONTENT

Supporting Information

The Supporting Information is available free of charge at https://pubs.acs.org/doi/10.1021/acsomega.4c02630.

Mesh independence verification (Figure S1), illustrations of the nanorod translocation through conventional single nanopipette configuration and dual-nanopipette configuration with a nanobridge (Figure S2), the magnitude of the electric field when nanorods translocate the nanopipette (Figure S3), ionic currents when nanorods translocate the nanopipette (Figure S4), spatial distributions of $(c_1^*-c_2^*)$ and the flow field around the nanorod (Figure S5), trajectories of the nanorod when $\sigma_w = -0.005$ C/m^2 and $\sigma_w = 0.005$ C/m^2 (Figure S6), the nanorod's y-component translational velocity, V_P^*, vs its location, y_P^*, under $\phi_0 = 0.1$ V and $\phi_0 = 10$ V when the initial location of the nanorod is $(x_{p0}^*, y_{p0}^*) = (25, 150)$ (Figure S7), the nanorod's y-component translational velocity, V_P^*, vs its location, y_P^*, under $\phi_0 = 10$ V when the initial location of the nanorod is $(x_{p0}^*, y_{p0}^*) = (25, 150)$. $C_0 = 10$ mM and $C_0 = 100$ mM (Figure S8), spatial distributions of $(c_1^*-c_2^*)$ and the flow field around the nanorod under $\phi_0 = 0.1$ V when the initial location of the nanorod is $(x_{p0}^*, y_{p0}^*) = (25, 150)$ (Figure S9), the results of b = 5 and 6 nm (Table S1), and ionic currents when nanorods translocate the dual-nanopipette with different σ_w (Figure S10) (PDF)

Trajectories of the nanorod (Supplementary Movies 1–3) (ZIP)

AUTHOR INFORMATION

Corresponding Author

Ning Hu − Key Laboratory of Biorheological Science and Technology, Ministry of Education and Bioengineering College, Chongqing University, Chongqing 400044, China; orcid.org/0000-0002-6902-3302; Email: huning@cqu.edu.cn

Authors

Xiaoling Zhang − School of Smart Health, Chongqing College of Electronic Engineering, Chongqing 401331, China; orcid.org/0000-0002-7412-2540

Yaqi Bai − Key Laboratory of Biorheological Science and Technology, Ministry of Education and Bioengineering College, Chongqing University, Chongqing 400044, China

Shiping Liu − School of Safety Engineering, Chongqing University of Science and Technology, Chongqing 401331, China

Jun Yang − Key Laboratory of Biorheological Science and Technology, Ministry of Education and Bioengineering College, Chongqing University, Chongqing 400044, China; orcid.org/0000-0001-6877-8677

Complete contact information is available at:
https://pubs.acs.org/10.1021/acsomega.4c02630

■ REFERENCES

(1) Branton, D.; Deamer, D. W.; Marziali, A.; Bayley, H.; Benner, S. A.; Butler, T.; Di Ventra, M.; Garaj, S.; Hibbs, A.; Huang, X.; Jovanovich, S. B.; Krstic, P. S.; Lindsay, S.; Ling, X. S.; Mastrangelo, C. H.; Meller, A.; Oliver, J. S.; Pershin, Y. V.; Ramsey, J. M.; Riehn, R.; Soni, G. V.; Tabard-Cossa, V.; Wanunu, M.; Wiggin, M.; Schloss, J. A. The potential and challenges of nanopore sequencing. *Nat. Biotechnol.* **2008**, *26*, 1146−1153.

(2) Dekker, C. Solid-state nanopores. *Nat. Nanotechnol.* **2007**, *2*, 209−215.

(3) Liu, Y.; Dong, X.; Chen, P. Biological and chemical sensors based on graphene materials. *Chem. Soc. Rev.* **2012**, *41*, 2283−2307.

(4) Abgrall, P.; Nguyen, N. T. Nanofluidic devices and their applications. *Anal. Chem.* **2008**, *80*, 2326−2341.

(5) Hou, X.; Guo, W.; Jiang, L. Biomimetic smart nanopores and nanochannels. *Chem. Soc. Rev.* **2011**, *40*, 2385−2401.

(6) Zhang, Z.; Wen, L.; Jiang, L. Bioinspired smart asymmetric nanochannel membranes. *Chem. Soc. Rev.* **2018**, *47*, 322−356.

(7) Howorka, S.; Siwy, Z. Nanopore analytics: sensing of single molecules. *Chem. Soc. Rev.* **2009**, *38*, 2360−2384.

(8) Zhang, S.; Yin, X.; Li, M.; Zhang, X.; Zhang, X.; Qin, X.; Zhu, Z.; Yang, S.; Shao, Y. Ionic Current Behaviors of Dual Nano- and Micropipettes. *Anal. Chem.* **2018**, *90*, 8592−8599.

(9) Clarke, J.; Wu, H. C.; Jayasinghe, L.; Patel, A.; Reid, S.; Bayley, H. Continuous base identification for single-molecule nanopore DNA sequencing. *Nat. Nanotechnol.* **2009**, *4*, 265−270.

(10) Wang, Y.; Zheng, D.; Tan, Q.; Wang, M. X.; Gu, L. Q. Nanopore-based detection of circulating microRNAs in lung cancer patients. *Nat. Nanotechnol.* **2011**, *6*, 668−674.

(11) Ma, W.; Xie, W.; Tian, R.; Zeng, X.; Liang, L.; Hou, C.; Huo, D.; Wang, D. An ultrasensitive aptasensor of SARS-CoV-2 N protein based on ion current rectification with nanopipettes. *Sens. Actuators, B* **2023**, *377*, 133075.

(12) Yu, R.-J.; Ying, Y.-L.; Hu, Y.-X.; Gao, R.; Long, Y.-T. Label-Free Monitoring of Single Molecule Immunoreaction with a Nanopipette. *Anal. Chem.* **2017**, *89*, 8203−8206.

(13) Zhang, S.; Liu, G.; Chai, H.; Zhao, Y.-D.; Yu, L.; Chen, W. Detection of alkaline phosphatase activity with a functionalized nanopipette. *Electrochem. Commun.* **2019**, *99*, 71−74.

(14) Lu, S. M.; Long, Y. T. Confined Nanopipette-A new microfluidic approach for single cell analysis. *TrAC, Trends Anal. Chem.* **2019**, *117*, 39−46.

(15) Daviddi, E.; Gaudin, L. F.; Bentley, C. L. Scanning electrochemical cell microscopy: High-resolution structure-property studies of mono- and polycrystalline electrode materials. *Curr. Opin. Electrochem.* **2022**, *34*, 101006.

(16) Takahashi, Y.; Kobayashi, Y.; Wang, Z.; Ito, Y.; Ota, M.; Ida, H.; Kumatani, A.; Miyazawa, K.; Fujita, T.; Shiku, H.; Korchev, Y. E.; Miyata, Y.; Fukuma, T.; Chen, M.; Matsue, T. High-Resolution Electrochemical Mapping of the Hydrogen Evolution Reaction on Transition-Metal Dichalcogenide Nanosheets. *Angew. Chem., Int. Ed.* **2020**, *59*, 3601−3608.

(17) Takahashi, Y.; Shevchuk, A. I.; Novak, P.; Murakami, Y.; Shiku, H.; Korchev, Y. E.; Matsue, T. Simultaneous Noncontact Topography and Electrochemical Imaging by SECM/SICM Featuring Ion Current Feedback Regulation. *J. Am. Chem. Soc.* **2010**, *132*, 10118−10126.

(18) Zheng, X.; Liu, J.; Li, M.; Hua, Y.; Liang, X.; Zhang, S.; Zhang, X.; Shao, Y. Dual-Nanopipettes for the Detection of Single Nanoparticles and Small Molecules. *Anal. Chem.* **2022**, *94*, 17431−17438.

(19) Chen, F.; Panday, N.; Li, X.; Ma, T.; Guo, J.; Wang, X.; Kos, L.; Hu, K.; Gu, N.; He, J. Simultaneous mapping of nanoscale topography and surface potential of charged surfaces by scanning ion conductance microscopy. *Nanoscale* **2020**, *12*, 20737−20748.

(20) Momotenko, D.; Page, A.; Adobes-Vidal, M.; Unwin, P. R. Write-Read 3D Patterning with a Dual-Channel Nanopipette. *ACS Nano* **2016**, *10*, 8871−8878.

(21) Shao, Y.; He, P.; Yu, Z.; Liang, X.; Shao, Y. Modulation of ionic current behaviors based on a dual-channel micro/nano-pipette with ternary-form-charged model. *J. Electroanal. Chem.* **2022**, *908*, 116089.

(22) Sharel, P. E.; Kang, M.; Wilson, P.; Meng, L.; Perry, D.; Basile, A.; Unwin, P. R. High resolution visualization of the redox activity of Li_2O_2 in non-aqueous media: conformal layer *vs.* toroid structure. *Chem. Commun.* **2018**, *54*, 3053−3056.

(23) Cadinu, P.; Kang, M.; Nadappuram, B. P.; Ivanov, A. P.; Edel, J. B. Individually Addressable Multi-nanopores for Single-Molecule Targeted Operations. *Nano Lett.* **2020**, *20*, 2012−2019.

(24) Zhang, X.; Song, J.; Li, Z.; Zheng, Y.-W.; Zhao, W.-W.; Chen, H.-Y.; Xu, J.-J. theta-Nanopipette for Single-Cell Resistive-Pulse Profiling of DNA Repair Proteins Accompanied by Drug Evaluation. *Nano Lett.* **2023**, *23*, 8249−8255.

(25) Cadinu, P.; Nadappuram, B. P.; Lee, D. J.; Sze, J. Y. Y.; Campolo, G.; Zhang, Y.; Shevchuk, A.; Ladame, S.; Albrecht, T.; Korchev, Y.; Ivanov, A. P.; Edel, J. B. Single Molecule Trapping and Sensing Using Dual Nanopores Separated by a Zeptoliter Nanobridge. *Nano Lett.* **2017**, *17*, 6376−6384.

(26) Cadinu, P.; Campolo, G.; Pud, S.; Yang, W.; Edel, J. B.; Dekker, C.; Ivanov, A. P. Double Barrel Nanopores as a New Tool for Controlling Single-Molecule Transport. *Nano Lett.* **2018**, *18*, 2738−2745.

(27) Shi, X.-M.; Xu, Y.-T.; Zhou, B.-Y.; Wang, B.; Yu, S.-Y.; Zhao, W.-W.; Jiang, D.; Chen, H.-Y.; Xu, J.-J. Electrochemical Single-Cell Protein Therapeutics Using a Double-Barrel Nanopipette. *Angew. Chem., Int. Ed. Engl.* **2023**, *62*, No. e202215801.

(28) Zhang, X.; Song, J.; Li, Z.; Zheng, Y. W.; Zhao, W. W.; Chen, H. Y.; Xu, J. J. θ-Nanopipette for Single-Cell Resistive-Pulse Profiling of DNA Repair Proteins Accompanied by Drug Evaluation. *Nano Lett.* **2023**, *23*, 8249−8255.

(29) McPherson, I. J.; Brown, P.; Meloni, G. N.; Unwin, P. R. Visualization of Ion Fluxes in Nanopipettes: Detection and Analysis of Electro-osmosis of the Second Kind. *Anal. Chem.* **2021**, *93*, 16302−16307.

(30) Xu, C.; Liu, Y.; Xiong, T. Y.; Wu, F.; Yu, P.; Wang, J. H.; Mao, L. Q. Dynamic Behavior of Charged Particles at the Nanopipette Orifice. *ACS Sens.* **2021**, *6*, 2330−2338.

(31) Li, T.; He, X.; Zhang, K.; Wang, K.; Yu, P.; Mao, L. Observing single nanoparticle events at the orifice of a nanopipet. *Chem. Sci.* **2016**, *7*, 6365−6368.

(32) Liu, Y.; Xu, C.; Gao, T.; Chen, X.; Wang, J.; Yu, P.; Mao, L. Sizing Single Particles at the Orifice of a Nanopipette. *ACS Sens.* **2020**, *5*, 2351−2358.

(33) Gao, T. A.; Xu, C.; Chen, M. L.; Wang, J. H.; Mao, L. Q.; Yu, P. Insights into Surface Charge of Single Particles at the Orifice of a Nanopipette. *Anal. Chem.* **2022**, *94*, 8187−8193.

(34) Zhang, X.; Xu, M.; Yang, J.; Hu, N. Ion Transport in pH-Regulated Double-Barreled Nanopores. *Anal. Chem.* **2022**, *94*, 5642−5650.

(35) Nouri, R.; Tang, Z.; Guan, W. Quantitative Analysis of Factors Affecting the Event Rate in Glass Nanopore Sensors. *ACS Sens.* **2019**, *4*, 3007−3013.

(36) Lan, W.-J.; Holden, D. A.; Liu, J.; White, H. S. Pressure-Driven Nanoparticle Transport across Glass Membranes Containing a Conical-Shaped Nanopore. *J. Phys. Chem. C* **2011**, *115*, 18445−18452.

(37) Lan, W.-J.; Holden, D. A.; Zhang, B.; White, H. S. Nanoparticle Transport in Conical-Shaped Nanopores. *Anal. Chem.* **2011**, *83*, 3840−3847.

(38) Lan, W.-J.; Kubeil, C.; Xiong, J.-W.; Bund, A.; White, H. S. Effect of Surface Charge on the Resistive Pulse Waveshape during Particle Translocation through Glass Nanopores. *J. Phys. Chem. C* **2014**, *118*, 2726−2734.

(39) Chinappi, M.; Yamaji, M.; Kawano, R.; Cecconi, F. Analytical Model for Particle Capture in Nanopores Elucidates Competition among Electrophoresis, Electroosmosis, and Dielectrophoresis. *ACS Nano* **2020**, *14*, 15816−15828.

(40) Liu, H.; Qian, S.; Bau, H. H. The effect of translocating cylindrical particles on the ionic current through a nanopore. *Biophys. J.* **2007**, *92*, 1164−1177.

(41) Ai, Y.; Beskok, A.; Gauthier, D. T.; Joo, S. W.; Qian, S. Z. dc electrokinetic transport of cylindrical cells in straight microchannels. *Biomicrofluidics* **2009**, *3*, No. 044110.

(42) Ai, Y.; Joo, S. W.; Jiang, Y. T.; Xuan, X. C.; Qian, S. Z. Transient electrophoretic motion of a charged particle through a converging-diverging microchannel: Effect of direct current-dielectrophoretic force. *Electrophoresis* **2009**, *30*, 2499−2506.

(43) Ai, Y.; Park, S.; Zhu, J. J.; Xuan, X. C.; Beskok, A.; Qian, S. Z. DC Electrokinetic Particle Transport in an L-Shaped Microchannel. *Langmuir* **2010**, *26*, 2937−2944.

(44) Ai, Y.; Qian, S. Electrokinetic particle translocation through a nanopore. *Phys. Chem. Chem. Phys.* **2011**, *13*, 4060−4071.